

1 **Understanding NMR relaxometry of partially water-saturated rocks**

2 **O. Mohnke, R. Jorand, C. Nordlund, N. Klitzsch**

3 Institute for Applied Geophysics and Geothermal Energy (GGE), E.ON Energy Research

4 Center (E.ON ERC), RWTH Aachen University, Mathieustrasse 10, 52074 Aachen

5

6 **Abstract**

7 Nuclear Magnetic Resonance (NMR) relaxometry measurements are commonly used to
8 characterize the storage and transport properties of water-saturated rocks. These assessments
9 are based on the proportionality of NMR initial signal amplitude and relaxation time to
10 porosity (water content) and pore size, respectively. Herein, pore shapes are usually assumed
11 to be spherical or cylindrical. However, the NMR response at partial water saturation for
12 natural sediments and rocks may differ strongly from the responses calculated for spherical or
13 cylindrical pores, because these pore shapes cannot account for water menisci remaining in
14 the corners of de-saturated angular pores. Therefore, we consider a bundle of pores with
15 triangular cross-sections. We introduce analytical solutions of the NMR equations at partial
16 saturation of these pores, which account for water menisci of de-saturated pores. After
17 developing equations that describe the water distribution inside the pores, we calculate the
18 NMR response at partial saturation for imbibition and drainage based on the deduced water
19 distributions.

20 For this pore model, NMR amplitude and NMR relaxation time at partial water saturation
21 strongly depend on pore shape even so the NMR relaxation time at full saturation only
22 depends on the surface to volume ratio of the pore. The pore-shape-dependence at partial
23 saturation arises from the pore shape and capillary pressure dependent water distribution in
24 pores with triangular cross-sections. Moreover, we show the qualitative agreement of the

- 25 saturation dependent relaxation time distributions of our model with those observed for rocks
- 26 and soils.

27 **1 Introduction**

28 Understanding multi-phase flow processes in porous rocks and soils is vital for addressing
29 a number of problems in geosciences such as oil and gas recovery or vadose zone processes,
30 which influence groundwater recharge and evaporation. Effective permeability, which is
31 defined as the permeability of a fluid in presence of another fluid, is the decisive parameter
32 for fluid transport, and depends on fluid saturation, wetting condition, and pore structure. In
33 addition, saturation history influences the fluid content and the effective permeability (for a
34 specific pressure), which are different for imbibition and drainage.

35 A method considered suitable for determining water content of rocks non-invasively is
36 nuclear magnetic resonance (NMR), because the NMR initial signal amplitudes are directly
37 proportional to the hydrogen content in the pore space, and the NMR relaxation times are
38 linked to the size of the water-containing pores in the rock. In a two-phase system of water
39 and air only the water contributes to the NMR signal response. Therefore, NMR is widely
40 used for estimating transport and storage properties of rocks and sediments (Kenyon, 1997;
41 Seevers 1966; Fleury et al., 2001; Arnold et al., 2006).

42 In recent years, several researchers have studied the relationship between NMR and
43 multiphase flow behavior on the pore scale to better understand and infer the storage and
44 transport properties of partially saturated rocks or sediments (e.g., Chen et al., 1994; Liaw et
45 al. 1996; Ioannidis et al., 2006; Jia et al., 2007; Al-Mahrooqi et al., 2006; Costabel and
46 Yaramanci, 2011, 2013; Talabi et al., 2009). As an extension of this research, we study the
47 relationship between the water distribution inside the pores of a partially saturated rock and
48 the system's NMR response by using bundles of pore with triangular cross-sections. While
49 Al-Mahrooqi et al. (2006) used a similar modeling approach to infer the wettability properties
50 in oil-water systems, this study investigates the evolution of the NMR relaxation-time spectra
51 during drainage and imbibition. For this purpose, we consider a capillary pore ensemble that

52 is partially saturated with water and air. Traditionally, the pores within this ensemble are
53 assumed to have a cylindrical geometry. Depending on pressure, cylindrical capillaries are
54 either water- or air-filled and thus they either contribute to an NMR response or they do not.
55 Consequently, the NMR relaxation times of partially water-saturated capillary pore bundles
56 always remain subsets of the fully saturated system's relaxation-time distribution, i.e., they
57 are a function inside the envelope of the distribution curve at full saturation (see Fig. 1).
58 However, in porous rocks, which are formed by the aggregation of grains, the pore geometry
59 is usually more complex (Lenormand et al., 1983; Ransohoff and Radke, 1987; Dong and
60 Chatzis, 1995) and may exhibit angular and slit-shaped pore cross-sections rather than
61 cylindrical capillaries or spheres (Fig. 2a). For example, in tight gas reservoir rocks Desbois
62 et al. (2011) found three types of pore shapes that are controlled by the organization of clay
63 sheet aggregates: i) elongated or slit-shaped, ii) triangular, and iii) multi-angular cross-
64 sections. The relaxation-time distribution functions derived from NMR measurements for
65 such partially saturated rocks are frequently found to be shifted towards shorter relaxation
66 times outside the original envelope observed for a fully saturated sample, (Fig. 2b) (e.g.,
67 Applied Reservoir Technology Ltd., 1996; Bird, et al., 2005; ; Jaeger et al., 2009; Jorand et
68 al., 2010; Stingaciu, 2010a,b; Costabel, 2011).

69 In angular pores, water will remain trapped inside the pore corners even if the gas entry
70 pressure is exceeded. Standard NMR pore models that assume cylindrical or spherical pore-
71 ensembles (e.g., Kenyon, 1997), however, do not account for such residual water (Blunt et
72 al., 2002; Tuller et al., 1999; Or and Tuller, 2000; Tuller and Or, 2001; Thern, 2014). To
73 overcome this limitation, we adopt a NMR modeling approach initially proposed and
74 discussed by Costabel (2011) and present numerical simulations and analytical solutions of
75 the NMR equations for partially saturated pores with triangular cross-sections to quantify
76 NMR signal amplitudes and relaxation times. The NMR response of a triangular capillary

77 during drainage and imbibition depends on the water distribution inside the capillary, which
78 is subject to pore shape and capillary pressure. Thus, in the next chapter we present the
79 relationship between capillary pressure and water distribution inside cylindrical and
80 triangular pore geometries during drainage and imbibition. For this purpose, the reduced
81 similar geometry concept introduced by Mason and Marrow (1991) is used. Subsequently,
82 based on the spatial water distribution, an analytical solution of the NMR diffusion equation
83 (Torrey, 1956; Brownstein and Tarr, 1979) for partially saturated triangular capillaries is
84 derived and tested by numerical simulations (Mohnke and Klitzsch, 2010). The derived
85 equations are used to study the influence of pore size distribution and pore shape of triangular
86 capillaries on the NMR response, in particular considering the effects of trapped water.
87 Finally, an approach for simulating NMR signals during imbibition and drainage of triangular
88 pore capillaries is introduced and demonstrated using synthetic pore size distributions.

89

90 **2 Results and discussion**

91 **2.1 Water distribution during drainage and imbibition in a partially saturated** 92 **triangular tube**

93 In a partially saturated pore space, a curved liquid-vapor interface called the arc meniscus
94 (AM) arises due to the pore's capillary forces. In addition, adsorptive forces between water
95 and matrix lead to the formation of a thin water film at the rock-air interface. Such water
96 films with a thickness typically below 20 nm (e.g., Toledo et al., 1990; Tokunaga and Wan,
97 1997) exhibit very short NMR relaxation times. Although water films to some extent may
98 influence transport properties and water distribution of a partially saturated porous system
99 (Tuller and Or, 2001), the contribution of the film volume to NMR amplitudes is very small
100 with respect to the NMR signal amplitudes arising from the water trapped in the menisci, i.e.,
101 $V_{\text{film}} \ll V_{\text{meniscus}}$. Therefore, for sake of simplicity, we neglect water films in his study.

102 In the following discussion, we consider a triangular capillary, initially filled with a
 103 perfectly wetting liquid, i.e., contact angle $\theta = 0^\circ$, which exhibits a constant interfacial
 104 tension σ ($\sigma_{\text{air-water}} = 73 \times 10^{-3} \text{ Nm}^{-1}$ at 20°C) and is under the assumption that gravity
 105 forces are weak and therefore can be neglected. The two-phase capillary entry pressure as
 106 derived by the MS-P method (Mayer and Stowe, 1965; Princen, 1969a, b, 1970) can be
 107 expressed by the Young-Laplace equation:

$$p_c = \frac{\sigma \cos \theta}{r_{\text{AM}}} = \frac{\sigma}{r_{\text{AM}}}, \quad (1)$$

108 where r_{AM} is the radius of the interface arc meniscus and p_c is the minimum pressure
 109 difference necessary for a non-wetting phase, i.e., air, to invade a uniformly wetted (tri-)
 110 angular tube filled with a denser phase, i.e., water (see Fig. 3a). Upon consideration of a
 111 pressure difference $p > p_c$, the non-wetting phase will begin to enter the pore and occupy the
 112 central portion of the triangle, whereas – separated by the three interface arc menisci of radius
 113 r_{AM} – the wetting fluid remains in the pore corners (Fig. 3a).

114 From an original triangle ABC , a new smaller triangle $A'B'C'$ of similar geometry with an
 115 inscribed circle of radius $r' = r_{\text{AM}} < R_0$ can be constructed by means of the reduced similar
 116 geometry concept as introduced by Mason and Morrow (1991) (Fig. 3b). To account for
 117 different transport mechanisms during imbibition and drainage of the denser wetting phase,
 118 Mason and Morrow (1991) introduced two different principal displacement curvatures with
 119 radii r_I and r_D , respectively.

120 During imbibition of a (tri-)angular pore, the radius of curvature r_{AM} increases until the
 121 separate arc menisci of the corners touch and the pore fills spontaneously (“snap off”). The
 122 critical radius of curvature r_I , which is equal to the radius of the pore’s inscribing circle, for
 123 the angular pore at “snap-off” pressure p_I is then given by

$$r_I = \frac{2A}{p}, \quad (2)$$

124

125 According to Eq. 2, the snap-off pressure depends on the geometry of the triangle only,
126 i.e., on its cross-sectional area A and perimeter P . In contrast, during drainage the threshold
127 radius of curvature $r_D = r_{AM}$, at which the center of the fully saturated angular capillary
128 spontaneously empties as a non-wetting fluid phase invades the pore, is given by

$$r_D = P \left[\frac{1}{2G} + \left(\frac{\pi}{G} \right)^{1/2} \right]^{-1}, \quad (3)$$

129 with $r_D < r_I$ and drainage threshold pressure $p_D > p_I$. The dimensionless and size-
130 independent factor $G = \frac{A}{P^2} \left(= \frac{A'}{P'^2} \right)$ reflects the shape of the triangle depending on its cross-
131 sectional area A and perimeter P (A' and P' refer to the reduced triangle), i.e., from near-slit-
132 shape ($\lim_{\gamma \rightarrow 0} G = 0$) to equilateral shape ($G = 0.048$). A detailed derivation of Eqs. 2 and 3
133 as a consequence of hysteresis between drainage and imbibition can be found in Mason and
134 Morrow (1991).

135 Note, that the permeability of a porous system of such triangular capillaries is strongly
136 influenced by the shape factor G . For single-phase laminar flow in a triangular tube the
137 hydraulic conductance g is given by the Hagen-Poiseuille formula

$$g = k \frac{A^2 G}{\mu} \quad (4)$$

138 with the cross-sectional area A , the shape factor G , the fluid viscosity μ , and k being a
139 constant accounting for the geometrical shape of the cross-section, e.g. $k = 0.5$ for circular
140 tubes and $k = 0.6$ for a tube with a cross-section of an equilateral triangle (Patzek and Silin,
141 2001). The hydraulic conductance of an irregular triangle is closely approximated by
142 equation 1 using the same constant k as for an equilateral triangle (Øren et al., 1998). Thus,

143 for a constant cross-sectional area the hydraulic conductance g of the pore is proportional to
 144 its shape factor G .

145 Combining Eqs. 1–3 with the concept of reduced similar geometry discussed above, the
 146 degree of water saturation (S_w) inside a single triangular tube with cross-sectional area A_0 ,
 147 perimeter P_0 , and radius R_0 of its inscribing circle at a given capillary pressure p_c during
 148 imbibition and drainage can be calculated according to

149

$$S_w^I(p, A_0, P_0) = \begin{cases} 1 & , p_c \leq p_I \quad (R_0 \leq r_I) \\ \frac{A_\Delta(p_c)}{A_0} & , p_c > p_I \quad (R_0 > r_I) \end{cases} \quad \text{(imbibition)} \quad (5)$$

150

$$S_w^D(p_c, A_0, P_0) = \begin{cases} 1 & , p_c < p_D \quad (R_0 < r_D) \\ \frac{A_\Delta(p_c)}{A_0} & , p_c \geq p_D \quad (R_0 \geq r_D) \end{cases} \quad \text{(drainage)} \quad (6)$$

151

152 The total area A_Δ of the triangular tube's water retaining corners, $\gamma_{1,2,3}$ (i.e., the gray
 153 areas in Figs. 4 and 5) is expressed by

$$A_\Delta(p_c) = \sum_{i=1}^3 A_{\gamma_i}(p_c), \quad (7a)$$

154 where

$$A_{\gamma_i}(p_c) = \left(\frac{1}{\tan \frac{\gamma_i}{2}} - \frac{(\pi - \gamma_i)}{2} \right) r_{AM}^2(p_c), \quad 0 < \gamma_i < \pi \quad (7b)$$

155 is the area of the triangle's i th water-filled corner (Tuller and Or, 1999). Consequently, the
 156 total effective area A_Δ still occupied by water is equal to the difference between the (reduced)
 157 triangular pore area \tilde{A} and the area πr_{AM}^2 of its respective inscribing circle (see Fig. 3). Above

158 equations can be simplified to $A_{\Delta} = (3\sqrt{3} - \pi) r_{AM}^2(p_c)$ when considering equilateral
159 triangles, i.e., $\gamma_{1,2,3} = \frac{\pi}{3}$. The radius $r_{AM}(p_c)$ of the reduced triangle's arc meniscus can be
160 directly calculated from Eq. 1. Calculated pressure-dependent water and gas distributions
161 during imbibition and drainage for an equilateral and arbitrary triangular capillary are shown
162 in Figs. 4a and 5a. The corresponding water retention curves plotted in Figs. 4b and 5b
163 illustrate the resulting hysteresis behavior of the partially saturated system and can be
164 subdivided into three parts: at low capillary pressures, i.e., $p_c < p_I$, the pore always remains
165 fully water-saturated. For the interval $p_I < p_c \leq p_D$, two separate behaviors are observed:
166 during imbibition, the water content gradually increases with increasing capillary pressure,
167 while during drainage the pore still remains fully saturated. For pressure levels $p_c \geq p_D$, both
168 drainage as well as imbibition exhibit the same gradual decrease of water saturation.

169 In the following section, analytical solutions for respective NMR responses that arise
170 from partially saturated arbitrary triangular tubes are derived and validated with numerical
171 simulations of the NMR diffusion equations.

172

173 **2.2 NMR response for triangular capillaries**

174 NMR relaxometry is commonly employed for petrophysical investigations of saturated
175 porous rocks in well-logging and laboratory studies. In this respect, the NMR method is a
176 unique geophysical tool, which delivers direct information about the water content and allows
177 to infer the pore-size distribution in rock samples or the subsurface. The measured NMR
178 relaxation signal $M(t)$ is constituted by superposition of all signal-contributing pores in a rock
179 sample (e.g., Coates et al., 1999; Dunn et al., 2002):

$$\frac{M(t)}{M_0} = \frac{1}{V_0} \sum_i^N \left(v_i \times \left(1 - e^{-t/T_{i,1}^{-1}} \right) \right), \quad (8)$$

180 where M_0 and V_0 are the equilibrium magnetization and total volume of the pore system,
 181 respectively. The saturated volume of the i th pore and its corresponding longitudinal
 182 relaxation constant are given by v_i and $T_{i,1}$, respectively.

183 Following derivations of Brownstein and Tarr (1979), the inverse of the longitudinal
 184 relaxation time T_1 is linearly proportional to the surface-to-volume ratio of a pore according
 185 to

$$T_1^{-1} = T_{1B}^{-1} + \rho_s \frac{S_a}{V}, \quad (9)$$

186 where T_{1B} is the bulk relaxation time of the free fluid and ρ_s is the surface relaxivity, a
 187 measure of how quickly protons lose their magnetization due to magnetic interactions at the
 188 fluid-solid interface, which can be attributed to paramagnetic ions at mineral grain surfaces. V
 189 and S_a are the pore's volume and active surface boundaries, respectively. In this context, an
 190 active boundary refers to an interfacial area, i.e., the pore wall, where $\rho > 0$ and, thus,
 191 enhanced NMR relaxation will occur as the molecules diffuse at the pore walls. This model,
 192 however, is based on the general assumption of a relaxation regime that is dominated by
 193 surface relaxation processes (*fast diffusion*), i.e., the fluid molecules move sufficiently fast
 194 and thus explore all parts of the pore volume with respect to the time scale ($\sim T_1$) of the
 195 experiment.

196 Upon consideration of a long (triangular) capillary, its surface-to-volume-ratio equals its
 197 perimeter-to-cross-section-ratio, i.e., $S/V = P/A$. Consequently, Eq. 9 can be written as

$$T_1^{-1} = T_{1B}^{-1} + \rho \frac{P_0}{A_0}, \quad (10)$$

198 where P_0 is the saturated tube's (active) perimeter and A_0 its cross-sectional area for a circular
 199 cross-section, $\frac{P_0}{A_0} = \frac{2}{r_0}$, with r_0 being the capillary radius. Hence, the relaxation rate of a fully
 200 saturated arbitrary triangular pore ABC can be expressed in terms of its shape factor G and
 201 perimeter P_0 :

$$T_1^{-1} = T_{1B}^{-1} + \frac{\rho}{G P_0} \left(= T_{1B}^{-1} + \rho \frac{L_{AB} + L_{BC} + L_{CA}}{L_{AB} L_{CA} \sin(\gamma_A)} \right) , \quad (11)$$

202 where L_{AB} , L_{BC} , and L_{AC} are the lengths of a triangle's sides and γ_A is the angle at corner A
 203 (see Fig. 3). As illustrated in Fig. 6, the relaxation times of a fully saturated pore decrease
 204 with decreasing pore shape factor G – and thus, decreasing hydraulic conductance – and
 205 increasing pore perimeter P . By reducing one angle from 60° to 0° while fixing another at
 206 60° , we increase P/A for a constant cross-sectional area A . In the special case of an
 207 equilateral triangular capillary, i.e., $P_0/A_0 = \frac{12}{\sqrt{3} L_0}$, Eq. 11 can be simplified to
 208

$$T_1^{-1} = T_{1B}^{-1} + \rho \frac{12}{\sqrt{3} L_0} . \quad (12)$$

209 Now we consider the previously discussed water-air system of a partially saturated
 210 equilateral triangular capillary. Here, the NMR signal will originate from the water retained
 211 at the corners. Replacing A_0 in Eq. 10 with an effective area A_γ or A_Δ as derived by Eqs. (7a)
 212 and b, respectively. A_Δ reflects the actual pore fraction that contributes to the NMR signal,
 213 i.e., the portion of the pore area A_0 that still remains occupied by water.

214 Supposing the air-water interface to be a passive boundary with respect to NMR surface
 215 relaxivity, i.e., $\rho = 0$, the effective active boundary is exclusively controlled by the pore wall
 216 segments ($\rho > 0$) in contact with water (wetting phase) (Fig. 7). Thus, the active perimeter of
 217 such a partially saturated triangular capillary is equal to its pressure-dependent reduced
 218 triangle's perimeter, $P'_\Delta(r^{LD}(p_c))$, according to

$$P_\Delta = \sum_{i=1}^{N=3} P_{\gamma_i} , \quad (13)$$

219 with

$$P_{\gamma_i} = 2 \frac{r_{AM}(p_c)}{\tan \frac{\gamma_i}{2}}, \quad 0 < \gamma_i < \pi \quad (14)$$

220 being the perimeter of the i th water-filled corner. Consequently, the NMR relaxation rates
 221 and NMR signal (amplitude) evolution during drainage and imbibition of a single equilateral
 222 triangular capillary can be expressed by
 223

$$T_{\Delta,1}^{-1} = \begin{cases} T_{1B}^{-1} + \rho \frac{P_0}{A_0}, & S_w^{I,D} = 1 \\ T_{1B}^{-1} + \rho \frac{P_{\Delta}^{I,D}(p_c, A_0, P_0)}{A_{\Delta}^{I,D}(p_c, A_0, P_0)}, & S_w^{I,D} < 1 \end{cases} \quad (15)$$

224 and

$$\frac{m(t)}{m_0} = S_w^{I,D}(p_c, A_0, P_0) \left(1 - e^{\frac{-t}{T_{\Delta,1}}} \right), \quad (16)$$

225 respectively. Illustrated in Fig. 8 is the pressure-dependent water distribution inside a single
 226 equilateral triangular capillary (with a side length of $1 \mu\text{m}$) during drainage (a) and
 227 corresponding evolution of longitudinal magnetization (b). As the water saturation is reduced
 228 with increasing pressure, both NMR amplitudes and relaxation times (c) decrease. Note that
 229 only a single characteristic relaxation time at each saturation degree is observed, since each
 230 corner has the same P_{γ}/A_{γ} , and consequently the same T_1 value.

231 In contrast, each water-filled corner of a partially saturated non-equilateral triangle, i.e.,
 232 $\gamma_1 \neq \gamma_2 \neq \gamma_3$, can have a different P_{γ}/A_{γ} ratio, and thus will show a different relaxation time
 233 and amplitude. As a result, depending on its individual shape, even a single partially saturated
 234 pore exhibits a multi-exponential NMR relaxation behavior based on Eq. (8) according to

$$\frac{m(t)}{m_0} = \frac{1}{A_0} \sum_{i=1}^{N=3} A_{\gamma_i}^{I,D} \left(1 - e^{\frac{-t}{T_{\gamma_i,1}}} \right), \quad (17)$$

235 with $T_{\gamma_{i,1}} = \frac{1}{T_{1B}} + \rho \frac{P_{\gamma_i}}{A_{\gamma_i}}$ and $\frac{A_{\gamma_i}^{1,D}}{A_0}$ being the characteristic relaxation time and amplitude
 236 contribution of the i th corner of the triangle, respectively. Figure 9 exemplifies such different
 237 multi-exponential relaxation behavior for a pore with a right triangle geometry with angles of
 238 ($\gamma_1 = 30^\circ, \gamma_2 = 60^\circ, \gamma_3 = 90^\circ$) and the same cross-sectional area as the equilateral pores in
 239 Fig. 8 (i.e., \sim NMR porosity).

240 To test the analytical (fast diffusion) models for partially saturated triangular capillaries
 241 derived above, the calculated longitudinal NMR relaxation times and amplitudes are
 242 compared to solutions obtained from 2D numerical simulations of the general NMR diffusion
 243 equation (Mohnke and Klitzsch, 2010):

$$\dot{m} = \left(D \nabla^2 - \frac{1}{T_B} \right) m, \quad (18)$$

244 with normalized initial values $m(\mathbf{r}, t = 0) = \frac{M_0=1}{A}$ and boundary conditions

$$D \mathbf{n} \nabla m \Big|_P = \rho_s m \Big|_P, \quad (19)$$

245 where m is the magnetization density, D the diffusion coefficient of water, T_B the bulk
 246 relaxation time, ρ_s the interface's surface relaxivity, \mathbf{n} the outward normal, and A and P the
 247 pore's cross-sectional area and perimeter, respectively. The above equations were solved
 248 numerically using finite elements (Mohnke and Klitzsch, 2010) to simulate the respective
 249 NMR relaxation data of the studied triangular geometries.

250 As shown in Fig. 10, analytically (+) calculated NMR relaxation data for drainage and
 251 imbibition for an equilateral triangular pore are in a very good agreement ($R^2 > 0.99$) with
 252 data obtained from numerical simulations (o).

253 The model was also validated for pores with arbitrary angles. Figure 11 illustrates 2D
 254 finite elements simulations using saturated pore corners with angles γ_i ranging from 5° to
 255 175° with equal active surface-to-volume ratios $P_{\gamma_i} / A_{\gamma_i} = \text{const.}$ and thus $T_{1,i} = \text{const.}$ The

256 simulations were compiled and compared to their respective analytical solutions. The ratios
257 of the numerical to the analytical model results for NMR amplitudes, i.e., NMR signal
258 amplitudes, A_γ , and relaxation times, $T_{1,\gamma}$ as function of corner aperture γ are shown and
259 confirm a near perfect correlation of $R^2 > 0.99$, with deviations generally less than 0.05 %.
260 In this regard, the slight increase in divergence of relaxation time ratios at acute and obtuse
261 angles can be attributed to numerical errors resulting from a decrease of the finite element's
262 grid quality due to extremely high or low x-to-y ratios at these apertures. Note that the above
263 model is applicable to any angular capillary geometry, such as square or octahedron.

264

265 **2.3 Simulated water retention curves and NMR relaxation data of partially saturated** 266 **pore distributions**

267 The goal of this section is to evaluate how pore shape affects the forward-modeled NMR
268 response of a partially saturated system of pores (a pore size distribution). As discussed
269 earlier, the NMR relaxation time of a single water-filled capillary pore is inversely
270 proportional to its surface-to-volume-ratio. Thus at full water saturation, the relaxation-time
271 distribution obtained from a multi-exponential NMR relaxation signal represents the pore-
272 size distribution of the rock. At partial water saturation, it is often assumed that the NMR
273 relaxation signal still represents the pore size distribution of the water saturated pores (e.g.,
274 Stingaciu, 2010b), which we are going to show is true for the cylindrical but not for (tri-)
275 angular pores.

276 In contrast to cylindrical pores, capillaries with (tri-)angular cross-sections may be partially
277 water-saturated during drainage or imbibition (cf. Fig. 8 and 9) because of the water
278 remaining in the corners. Thus, they show a different water retention behavior and the
279 “desaturated” pores, i.e. their arc menisci, contribute to the NMR signal. Consequently, with
280 increasing pressure (i.e. decreasing water saturation) the NMR relaxation behavior of the

281 partially water-saturated triangular capillary pore bundle successively shifts to signal
282 contributions with shorter relaxation times reflecting the fast relaxation of residual water
283 trapped in the pore corners (Figure 12). This behavior in angular pore geometries is
284 demonstrated in Figure 13. Here, the NMR relaxation components for a fully (blue line) and
285 partially saturated (red and green) distribution of triangular capillaries are plotted. The green
286 and red peaks show the signals of the residual water in the pore corners. Following from the
287 reduced geometry concept the remaining water in the corners has the same size and shape,
288 i.e., the same NMR relaxation time, for all pores independent on their size but dependent on
289 pressure. Therefore with decreasing saturation, i.e., increasing pressure, the NMR signal of
290 the arc menisci increases and shifts towards smaller relaxation times. If the non-wetting phase
291 (air) has entered all capillaries, only one single relaxation time remains for the pore bundle of
292 equilateral triangles. For arbitrarily shaped triangular pores, three relaxation times would
293 remain for the de-saturated pore system. Hence, the concept of a relaxation time distribution
294 assumed in conventional NMR inversion and interpretation approaches would be no longer
295 valid.

296

297 All the same, we apply the concept of fitting multi-exponential relaxation time distributions
298 to NMR transients calculated for pore bundles of circular and equilateral triangle cross-
299 sections to study how pore shape affects the typically-shown relaxation time distributions.

300 Water drainage and imbibition with water as wetting and air as non-wetting fluid were
301 investigated by simulating water retention curves and corresponding NMR relaxation signals
302 for a log-normal distributed pore size ensemble as shown in Figure 14.

303 Herein, to clarify the subsequent discussion we focused on the equilateral triangular
304 capillary model. Note, that other angular pore shapes (e.g., right angular triangles or squares)
305 will exhibit a similar behavior. Capillary pressure curves presented in Figure 15a were

306 calculated from Eq. 1, 4, and 5 for pore bundles with circular and equilateral triangle cross-
307 sections. In contrast to water retention curves calculated for the cylindrical capillary model
308 significant hysteresis between drainage and imbibition can be observed for the triangular
309 capillary model, i.e. in terms of initial amplitudes (=saturation) and respective mean
310 relaxation times (Figure 15b). Corresponding NMR T_1 relaxation (saturation recovery)
311 signals shown in Figure 15c, d and e were calculated using a uniform surface relaxivity of
312 $\rho_s = 10 \mu\text{m/s}$ and water bulk relaxation $T_{1,bulk} = 3 \text{ s}$.

313 The NMR T_1 relaxation signals were simulated for 20 saturation levels of the drainage
314 and imbibition curves ranging from $S = 100\%$ to $S < 1 \%$ water saturation. The corresponding
315 relaxation time distributions (Figure 15f-h) of the NMR T_1 transients were determined by
316 means of a regularized multi-exponential fitting using a nonlinear least squares formulation
317 solved by the Levenberg-Marquardt approach (e.g., Marquardt, 1963; Mohnke, 2010).
318 Inverse modeling results of NMR data calculated for the drainage branches using the
319 cylindrical capillary bundle (Fig. 15f) exhibit a shift of the distribution's maximum towards
320 shorter relaxation times with decreasing saturation (i.e., increasing pressure). As anticipated,
321 the derived distribution functions remain inside the envelope of the relaxation-time
322 distribution curve at full saturation (see also Fig. 1a).

323 In contrast, inversion results for equilateral triangular capillary ensembles (Fig. 15f-h) –
324 both for imbibition and drainage – show a similar shift to shorter relaxation times with
325 decreasing saturation but also move outside the initial distribution at full saturation due to
326 NMR signals originating from trapped water in the pore corners of the desaturated triangular
327 capillaries. The effect of the pore corners on relaxation time at low saturations is also
328 recognizable when comparing the (geometric) mean relaxation times, normalized to the
329 values observed at full saturation (Fig. 15b): Both, the drainage and the imbibition hysteresis

330 branch of the triangular pore bundle show smaller mean relaxation times than the cylindrical
331 pore bundle.

332 In conclusion, the calculated inverse models for the triangular capillary bundle
333 qualitatively agree with the behavior of the inverted NMR relaxation-time distributions at
334 partial saturation that are frequently observed in experimental data, e.g., of the Rotliegend
335 sandstone shown in Fig. 2.

336 **3 Summary and conclusions**

337 Experimental NMR relaxometry data and corresponding relaxation-time distributions
338 obtained at partial water/air saturation were explicated by a modification of conventional
339 NMR pore models using triangular cross-sections. An analytical solution for calculating
340 surface-dominated (fast diffusion) NMR relaxation signals in fully and partially saturated
341 arbitrary angular capillaries was introduced and validated by numerical simulations.

342 Shape and size of triangular pores strongly influence both NMR and flow properties. The
343 NMR relaxation time depends on the surface-to-volume ratio, which again depends on shape
344 when considering angular pore capillaries. However, at partial saturation, the pore shape even
345 more influences the water distribution inside the pore system, and thus the NMR signal. In
346 contrast to cylindrical capillaries, angular capillaries also contribute to the NMR signal after
347 desaturation of the pore due to water remaining in the corners.

348 In this regard, non-equilateral triangular capillaries at partial saturation exhibit a three-
349 exponential relaxation behavior due to different perimeter-to-surface (= surface-to-volume)
350 ratios of the water in the pore corners whereas the relaxation time of the trapped water in the
351 corners depends on pressure (but not on pore size). Furthermore, the shape and size of the
352 triangular pores strongly influence both NMR and hydraulic properties. The NMR relaxation
353 time depends on the surface-to-volume ratio (not on pore shape), while the water distribution
354 inside the pore system, at partial saturation, is strongly influenced by the shape of the pore.

355 Thus, the NMR signal at partial saturation is affected by not only the surface-to-volume ratio,
356 but by the pore shape as well.

357 Moreover, we studied the NMR response of a triangular pore bundle model by jointly
358 simulating water retention curves for drainage and imbibition and the corresponding NMR
359 T_1 relaxometry data. With decreasing water saturation, the simulated NMR relaxation
360 distributions shift towards shorter relaxation times below the initial distribution envelope at
361 full saturation, which is principally in agreement with the relaxation behavior observed in
362 experimental NMR data from rocks.

363 Ongoing research will include implementation of the introduced approach in an inverse
364 modeling algorithm for NMR data obtained on partially saturated rocks to predict absolute
365 and relative permeability at laboratory and borehole scales. Without considering angular
366 pores the NMR signal of trapped water cannot be explained, i.e., using the classical approach
367 of circular capillaries one cannot find a pore size distribution which explains the relaxation
368 time distributions at all saturations sufficiently (e.g., Mohnke, 2014). On the other hand,
369 angular pore models can account for the trapped water and thus overcome the limitation of
370 the classical approach. Moreover, following the approach of Mohnke (2014) but considering
371 angular pores we strive for estimating surface relaxivity, pore size distribution, and pore
372 shape by jointly inverting NMR data at different saturations. Based on the obtained pore size
373 distribution and triangle shape we expect to improve the prediction of the absolute and
374 relative permeabilities considerably.

375

376 **Acknowledgements**

377 The study was supported by the German Research Foundation (DFG) in the framework of
378 the Transregional Collaborative Research Centre 32 (SFB TR 32) and Wintershall AG in the
379 framework of Wintershall Tight Gas Consortium at RWTH Aachen University.

381 **References**

- 382 Al-Mahrooqi, S. H., Grattoni, C. A., Muggeridge A. H., Zimmermann, R. W., and Jing, X.
383 D.: Pore-scale modelling of NMR relaxation for the characterization of wettability, J.
384 Petrol. Sci. Eng., 52, 172–186, 2006.
- 385 Applied Reservoir Technology Ltd.: The NMR Sandstone Rock Catalogue, Long Melford,
386 Suffolk, U.K., 1996.
- 387 Arnold, J., Clauser, C., Pechnig, R., Anferova, S., Anferov, V., and Blümich, B.: Porosity and
388 Permeability from Mobile NMR Core-Scanning, Petrophysics, 47, 306–314, 2006.
- 389 Bird, N.R.A., Preston, A. R., Randall, E. W., Whalley, W.R. and Whitmore, A.P.:
390 Measurement of the size-distribution of water-filled pores at different matric potentials by
391 STRAFI-NMR relaxation-time measurements. European Journal of Soil Science. 56: 135-
392 143, 2005.
- 393 Brownstein, K., and C. Tarr, C. (1979), Importance of classical diffusion in NMR studies of
394 water in biological cells, Phys. Rev. A, 19, 2446–2453, 1979.
- 395 Chen, S., Liaw, H. K., and Watson, A. T.: Measurements and analysis of fluid saturation-
396 dependent NMR relaxation and linebroadening in porous media, Magn. Reson. Imaging,
397 12(2), 201–202, 1994.
- 398 Coates, G. R., Xiao, L., and, Prammer, M. G.: NMR Logging Principles and Applications,
399 Halliburton Energy Services, Houston, TX, 234 pp., 1999.
- 400 Costabel, S.: Nuclear magnetic resonance on laboratory and field scale for estimating
401 hydraulic parameters in the vadose zone, PhD thesis, Berlin University of Technology,
402 2011. (opus4.kobv.de/opus4-tuberlin/files/3173/costabel_stephan.pdf) Costabel, S. and
403 Yaramanci, U.: Relative hydraulic conductivity in the vadose zone from magnetic
404 resonance sounding - Brooks-Corey parameterization of the capillary fringe, Geophysics,
405 76(3), G61–G71, doi:10.1190/1.3552688, 2011.

406 Costabel, S. and Yaramanci, U.: Estimation of water retention parameters from nuclear
407 magnetic resonance relaxation time distributions, *Water Resour. Res.*, 49(4), 2068–2079,
408 doi:10.1002/wrcr.20207, 2013.

409 Desbois, G., Urai, J. L., Kukla, P. A., Konstanty, J., and Baerle, C.: High-resolution 3D fabric
410 and porosity model in a tight gas sandstone reservoir: A new approach to investigate
411 microstructures from mm- to nm-scale combining argon beam cross-sectioning and SEM
412 imaging, *J. Petrol. Sci. Eng.*, 78, 243–257, doi:10.1016/j.petrol.2011.06.004, 2011.

413 Dong, M. and Chatzis, I.: The imbibition and flow of a wetting liquid along the corners of a
414 square capillary tube, *J. Colloid Interface Sci.*, 172, 278–288, 1995.

415 Dunn K. J., Bergman D. J., and LaTorraca G. A.: *Nuclear Magnetic Resonance:
416 Petrophysical and Logging Applications*, Pergamon: Elsevier Science, Amsterdam, 2002.

417 Finjord, J., Hiorth, A., a Lad, U. H., and Skjaeveland, S. M.: NMR for equilateral triangular
418 geometry under conditions of surface relaxivity - analytical and random walk solution,
419 *Transport Porous Med.*, 69, 33–53. arXiv:cond-mat/0508412v2, 2006.

420 Fleury, M., Deflandre F., and Godefroy, S.: Validity of permeability prediction from NMR
421 measurements, *CR. Acad. Sci. Series IIC – Chemistry*, 4, 869–872, doi:10.1016/S1387-
422 1609(01)01343-3, 2001.

423 Ioannidis, M., Chatzis, I., Lemaire, C., and Perunarkilli, R.: Unsaturated hydraulic
424 conductivity from nuclear magnetic resonance measurements, *Water Resour. Res.*, 42(7),
425 W07201, 6 pages, doi:10.1029/2006WR004955, 2006.

426 Jaeger, F., Bowe, S., van As, H., and Schaumann, G. E. (2009). Evaluation of ^1H NMR
427 relaxometry for the assessment of pore size distribution in soil samples. *European Journal of
428 Soil Science*, 60:1052 – 1064.

429 Jia, P., Dong, M., and Dai, L.: Threshold pressure in arbitrary triangular tubes using RSG
430 concept for all wetting conditions, *Colloid. Surface A*, 302, 88–95, 2007.

431 Kenyon, W.: Petrophysical principles of applications of NMR logging, *Log Anal.* 38(2), 21–
432 43, 1997.

433 Kleinberg, R.L.: Utility of NMR T2 distributions, connection with capillary pressure, clay
434 effect, and determination of the surface relaxivity parameter ρ_2 , *Magn. Reson. Imaging*,
435 14(7), 761–767. doi: 10.1016/S0730-725X(96)00161-0, 1996.

436 Lenormand R., Zarcone C., Sarr, A.: A Mechanisms of the displacement of one fluid by
437 another in a network of capillary ducts, *J. Fluid Mech.*, 135, 337–353, 1983.

438 Liaw, H.-K., Kulkarni, R., Chen, S., and Watson, A.T.: Characterization of fluid distributions
439 in porous media by NMR techniques, *AIChE J.*, 42(2), 538–546, doi:
440 10.1002/aic.690420223, 1996.

441 Marquardt, D. W.: An Algorithm for the Least-Squares Estimation of Nonlinear Parameters,
442 *Siam J. Appl. Math.*, 11(2), 431–441, 1963.

443 Mason, G. and Morrow, N. R.: Capillary behavior of a perfectly wetting liquid in irregular
444 triangular tubes, *J. Colloid. Interf. Sci.*, 141, 262–274, 1991.

445 Mayer, R. P., and Stowe, R. A.: Mercury porosimetry-breakthrough pressure for penetration
446 between packed spheres, *J. Colloid. Interf. Sci.*, 20, 893–911, 1965.

447 Mohnke, O.: Improved forward and inverse modelling of Surface NMR relaxation signals
448 using multi-exponential decomposition, Ph.D. thesis, Technical University Berlin, Berlin,
449 2010.

450 Mohnke, O. and Klitzsch, N.: Microscale Simulations of NMR Relaxation in Porous Media
451 Considering Internal Field Gradients, *Vadose Zone J.*, 9, 846–857,
452 doi:10.2136/vzj2009.0161, 2010.

453 Øren, P. E., S. Bakke, and O. J. Arntzen, Extending predictive capabilities to network
454 models, *SPE Journal*, 3, 324-336, 1998.

455 Or, D. and Tuller, M.: Flow in unsaturated fractured porous media: Hydraulic conductivity of
456 rough surfaces. *Water Resour. Res.*, 36(5), 1165–1177, doi:10.1029/2000WR900020,
457 2000.

458 Patzek, T. W., and D. B. Silin, Shape factor and hydraulic conductance in noncircular
459 capillaries I. One-phase creeping flow, *Journal of Colloid and Interface Science*, 236,
460 295-304, 2001.

461 Princen, H. M.: Capillary phenomena in assemblies of parallel cylinders I. Capillary rise
462 between 2 cylinders, *J. Colloid. Interf. Sci.*, 30, 69–75, 1969a.

463 Princen, H. M.: Capillary phenomena in assemblies of parallel cylinders II. Capillary rise in
464 systems with more than 2 cylinders, *J. Colloid. Interf. Sci.*, 30, 359–371, 1969b.

465 Princen, H. M.: Capillary phenomena in assemblies of parallel cylinders III. Liquid columns
466 between horizontal parallel cylinders, *J. Colloid. Interf. Sci.*, 34, 171–184, 1970.

467 Ransohoff, T. C., and Radke, C. J.: Laminar flow of a wetting liquid along the corners of a
468 predominantly gas-occupied noncircular pore, *J. Colloid Interface Sci.*, 121, 392–401,
469 1987.

470 Seevers, D. O.: A nuclear magnetic method for determining the permeability of sandstones,
471 *Society of Professional Well Log Analysts*, vol. 6, paper L, Houston, Texas, 1966.

472 Stingaciu, L. R.: Characterization of natural porous media by NMR and MRI techniques:
473 High and low magnetic field studies for estimation of hydraulic properties, Ph.D. thesis,
474 RWTH Aachen, URL: <http://darwin.bth.rwth-aachen.de/opus3/volltexte/2010/3392/>,
475 2010a (accessed on 06/30/2014).

476 Stingaciu, L. R., Weihermüller, L., Haber-Pohlmeier, S., Stapf, S., Vereecken, H., and
477 Pohlmeier, A.: Determination of pore size distribution and hydraulic properties using
478 nuclear magnetic resonance relaxometry: A comparative study of laboratory methods.
479 *Water Resour. Res.*, 46, 1–11, doi:10.1029/2009WR008686, 2010b.

480 Talabi, O., AlSayari, S. Iglauer, I., and Blunt, J.: Pore-scale simulation of NMR response, J.
481 Petrol. Sci. Eng., 67, 168–178, 2009.

482 Thern, H.: Examining the fluid film model in porous media by NMR rock catalogue data,
483 Symposium of the Society of Core Analysts, Avignon, France, paper SCA2014-051.

484 Tokunaga, T. K. and Wan, J.: Water film flow along fracture surfaces of porous rock, Water
485 Resour. Res., 33(6), 1287–1295, doi:10.1029/97WR00473, 1997.

486 Toledo, P. G., Novy, R. A., Davis, H. T., and Scriven, L. E.: Hydraulic Conductivity of
487 Porous Media at Low Water Content, Soil Sci. Soc. Am. J., 54, 673–679,
488 10.2136/sssaj1990.03615995005400030007x, 1990.

489 Torrey, H. C.: Bloch equations with diffusion terms, Phys. Rev., 104(3), 563–565,
490 doi:10.1103/PhysRev.104.563, 1956.

491 Tuller, M., Or, D., and Dudley, L.M.: Adsorption and capillary condensation in porous media
492 - liquid retention and interfacial configurations in angular pores, Water Resour. Res.,
493 35(7), 1949–1964, doi: 10.1029/1999WR900098, 1999.

494 Tuller, M. and Or, D.: Hydraulic conductivity of variably saturated porous media: Film and
495 corner flow in angular pore space, Water Resour. Res., 37(5), 1257–1276, DOI:
496 10.1029/2000WR900328, 2001.

497 FIGURES

498

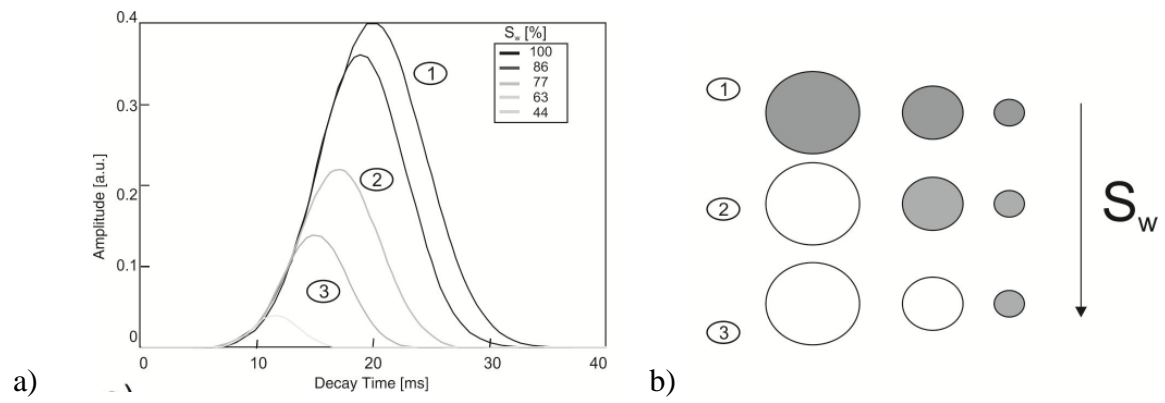
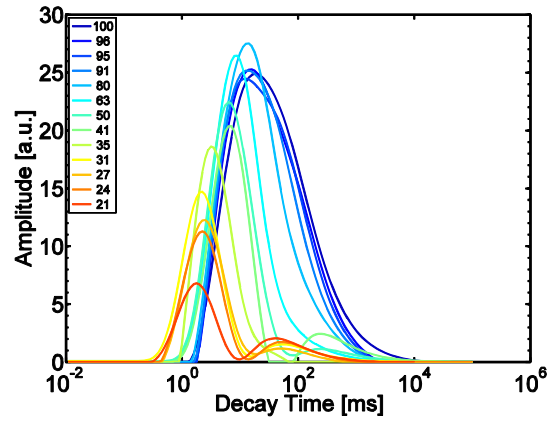
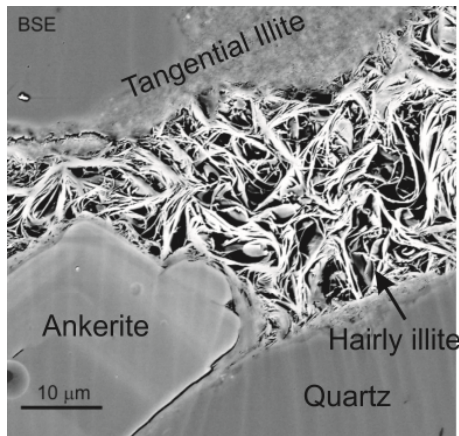


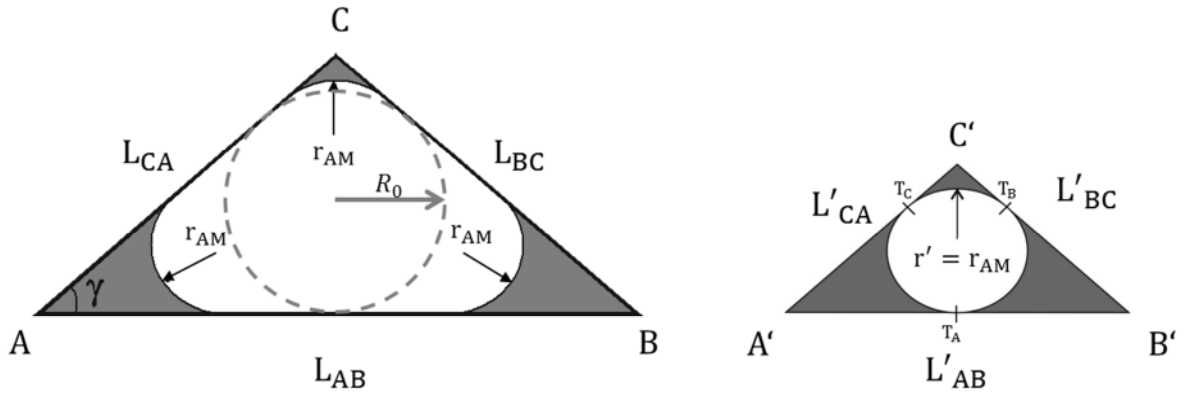
Figure 1. a) NMR decay time distributions at different water saturation levels for a classical cylindrical capillary pore distribution. b) Concept sketch of saturated (gray) and de-saturated capillaries, e.g., during drainage.



a)

b)

Figure 2. a) Complex pore structure of a Rotliegend tight gas sandstone. Pore spaces are filled with tangential and hairy illite and exhibit different pore types with elongated or slit-shaped, triangular, and multi-angular cross-sections. b) T_1 decay time distributions calculated from inverse Laplace transform performed on Rotliegend sandstone (porosity 13%, permeability 0.1 mD) at different water saturations ($S_w = 21\% - 100\%$).



a)

b)

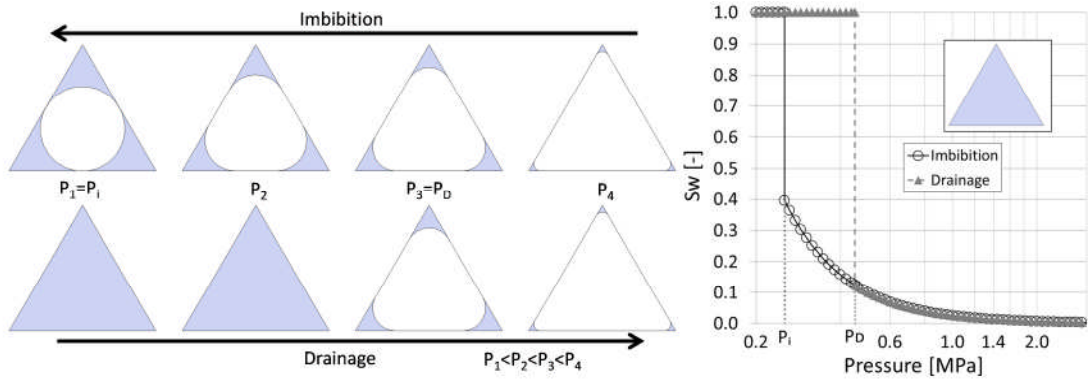
Figure 3. Cross-sections of a partially saturated triangular tube. Arc meniscus of radius r_{AM} separates invading non-wetting phase (white) from adsorbed wetting phase (gray). a)

Original triangle ABC with side lengths L_{AB}, L_{BC}, L_{CA} , and radius R_0 of its inscribing circle.

b) Reduced triangle $A'B'C'$ of similar geometry. The wetting phase resides in the three corners (gray) with $r' = r_{AM}$ being the radius of both the three interface arc menisci of ABC and of the inscribing circle of $A'B'C'$

501

502



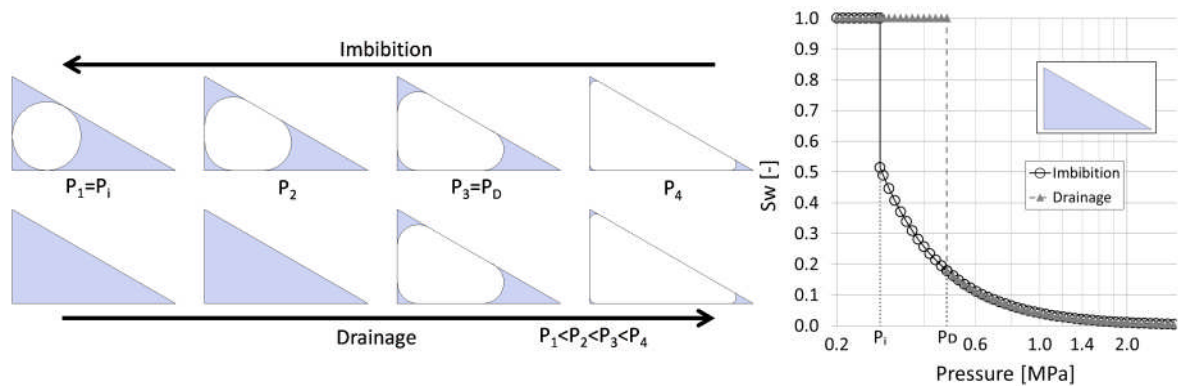
a)

b)

Figure 4. a) Modeled distribution of water (gray) and gas (white) phases in an equilateral triangular tube with a side length of $1 \mu\text{m}$ during imbibition (top) and drainage (bottom). b) Water saturation versus capillary pressure during imbibition (\circ) and drainage (\blacktriangle).

503

504



a)

b)

Figure 5. a) Modeled distribution of water (gray) and gas (white) phases in a right-angled triangular capillary ($G = 0.39$) with side lengths $L = 1, 0.81, 0.58 \mu\text{m}$, and perimeter $P = 2.39 \mu\text{m}$ during imbibition (top) and drainage (bottom). b) Water saturation versus capillary pressure during imbibition (\circ) and drainage (\blacktriangle).

505

506

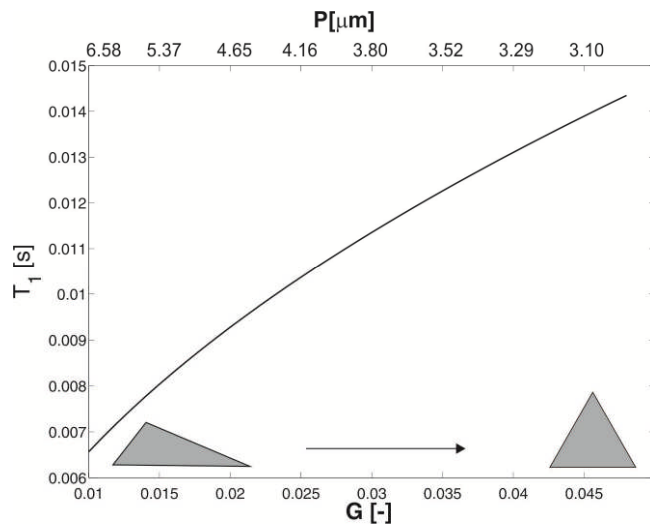


Figure 6. Longitudinal relaxation times T_1 of fully saturated triangular pores with constant cross-sectional area $A = 4.33 \cdot 10^{-13} \text{ m}^2$ versus shape factor $G = \frac{A}{P^2}$ and perimeter P . NMR parameters: $\rho_s = 10 \frac{\mu\text{m}}{\text{s}}$, $T_{1B} = 3 \text{ s}$.

507

508

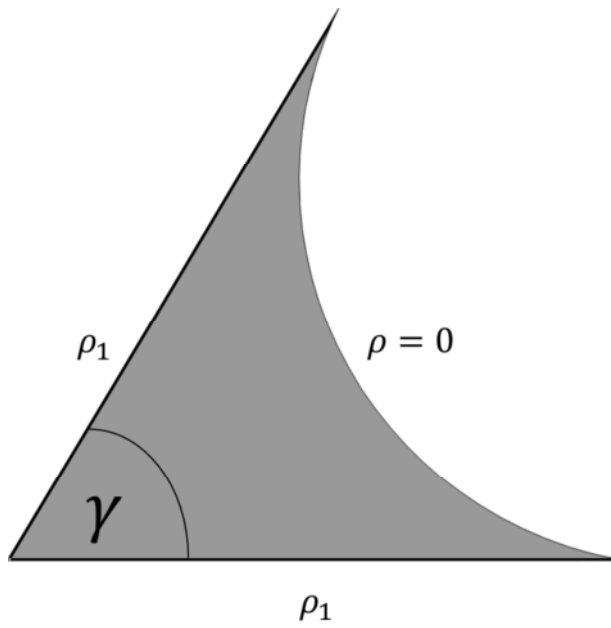


Figure 7. Saturated corner with active boundaries, i.e., $\rho_s = \rho_1 > 0$ at the corner's perimeter P_γ and a passive boundary at the air-water interface (meniscus), i.e., $\rho_s = \rho = 0$.

509

510

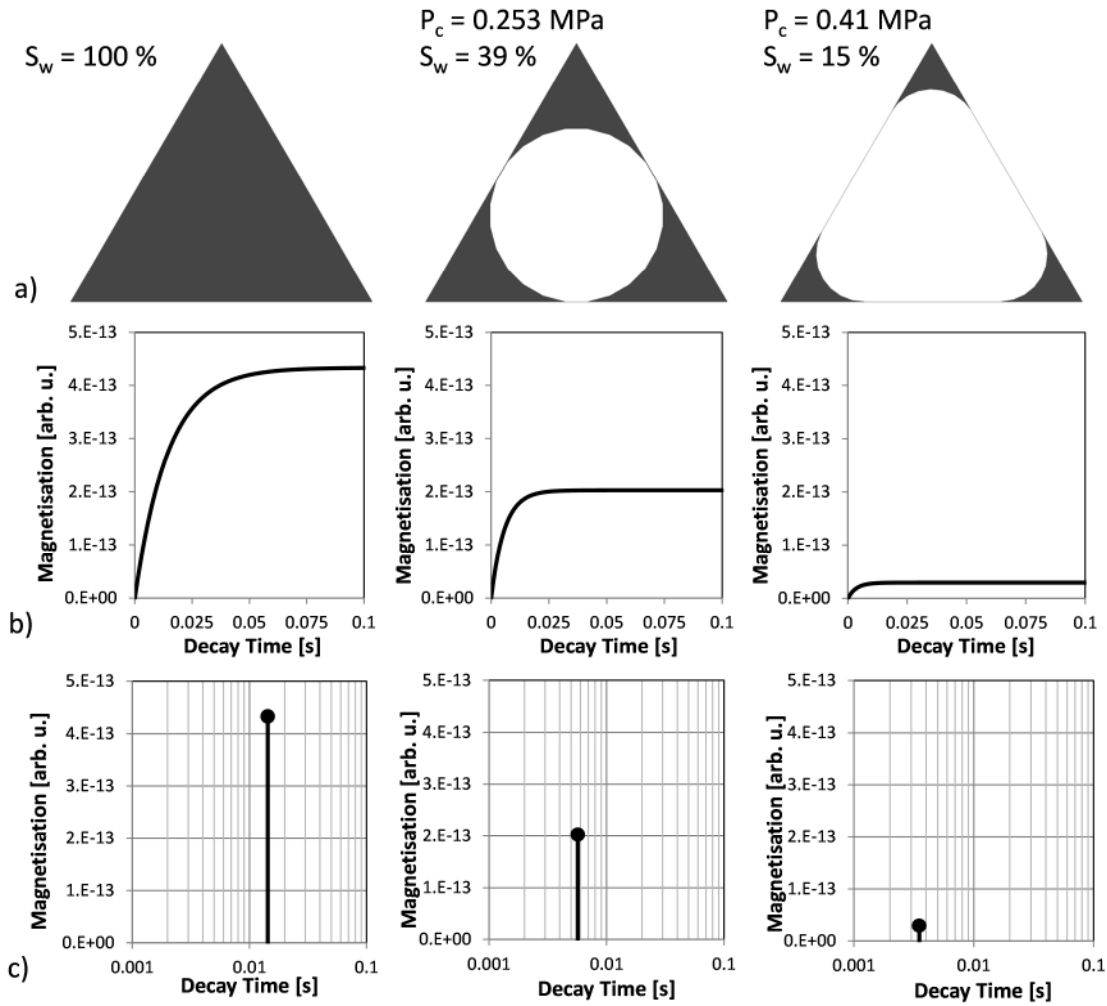


Figure 8. Water (black) and air (white) distributions within a triangular pore ($A_0 = 4.33 \cdot 10^{-13} \text{ m}^2$, $\rho_s = 10^{-5} \text{ m/s}$) at different capillary pressures for imbibition (a) with corresponding evolution of the (longitudinal) magnetization (b) and NMR T_1 relaxation times (c).

511

512

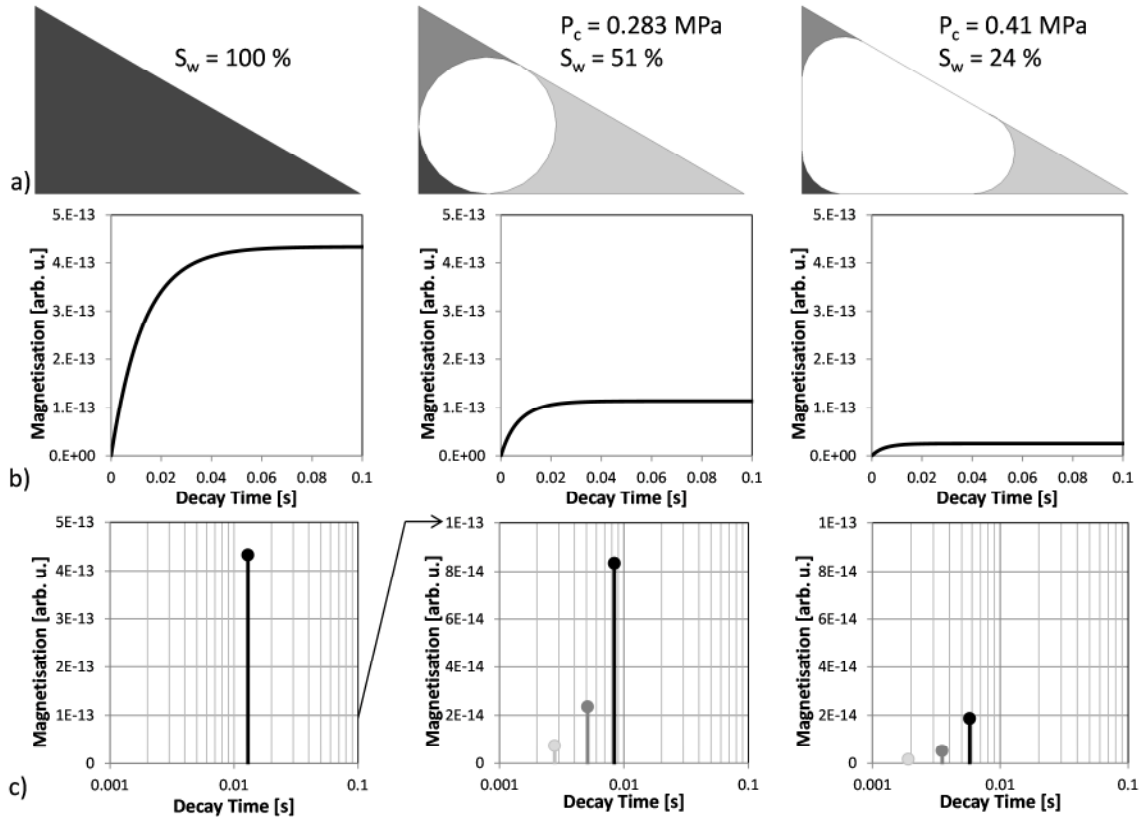


Figure 9. Water (black and grays) and air (white) distributions within a right-angled triangular pore ($A_0 = 4.33 \cdot 10^{-13} \text{ m}^2$, $\rho_s = 10^{-5} \text{ m s}^{-1}$) at different capillary pressures for imbibition (a) with corresponding evolution of the (longitudinal) magnetization (b) and NMR T_1 relaxation times (c).

513

514

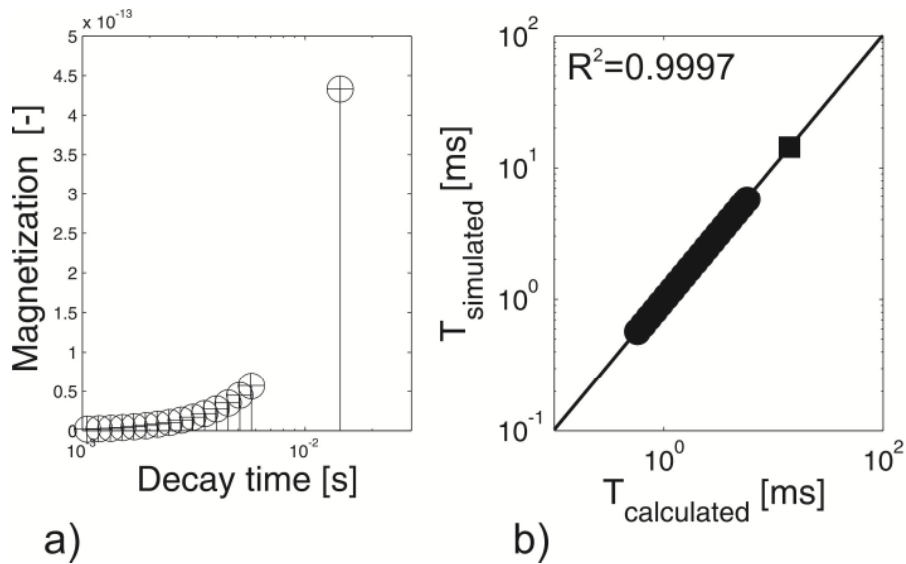


Figure 10. NMR response of an equilateral triangular capillary pore model (with a side length of $1 \mu\text{m}$). a) Magnetization versus T_1 decay time data of numerical (\circ) and analytical solutions ($+$) for all applied pressure levels. b) Cross-plot of numerically simulated and analytically calculated longitudinal T_1 decay times at partial (\bullet) and full water saturation (\blacksquare).

A corresponding water saturation versus capillary pressure diagram is shown in Fig. 4.

515

516

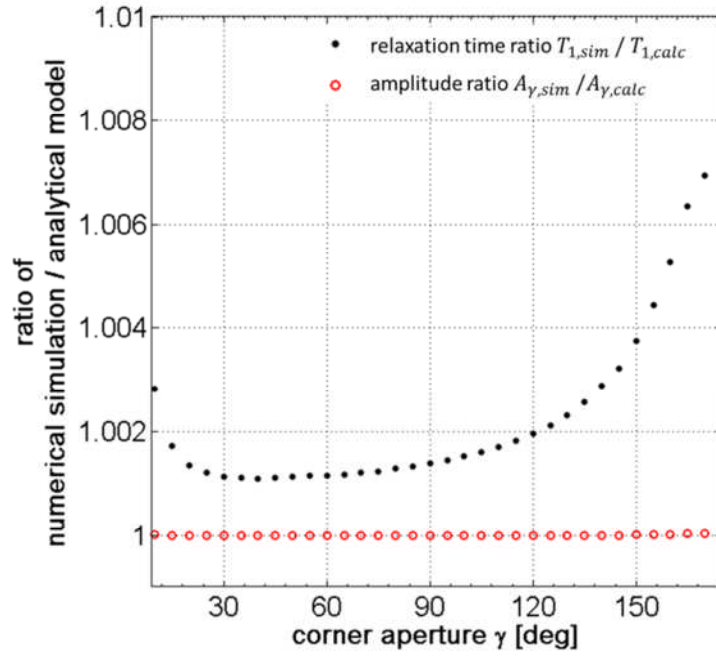


Figure 11. Comparison of analytical and calculated NMR relaxometry data originating from saturated pore corners (e.g. see Fig. 7) of varying apertures ($5^\circ < \gamma < 175^\circ$) and equal

active surface-to-volume ratio $\frac{P_{Y_i}}{A_{Y_i}} = const.$ (NMR model parameters; $T_{1B} = 3s$,

$D = 2.5 \cdot 10^{-9} \text{ m}^2 \text{ s}^{-1}$, $\rho_s = 10 \mu\text{m s}^{-1}$).

517

518

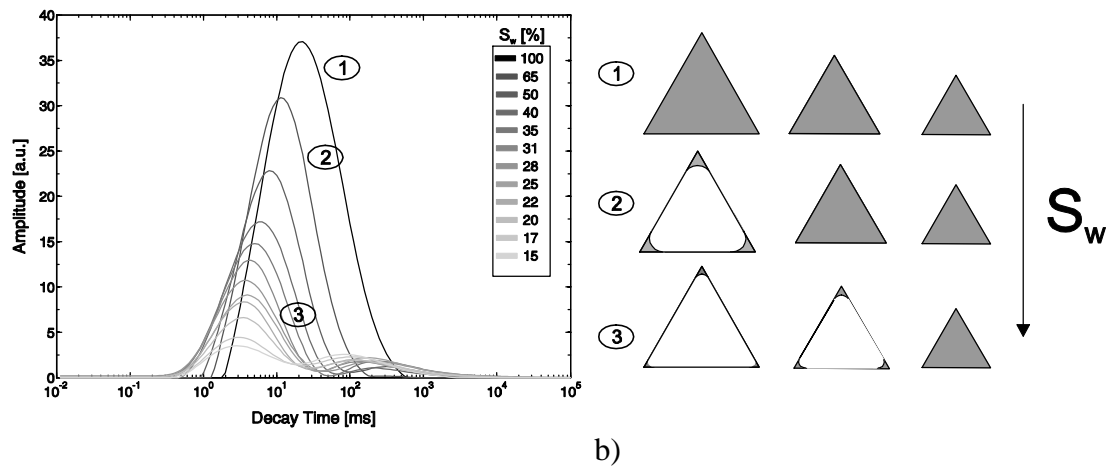


Figure 12. a) NMR decay time distributions at different water saturation levels for a pore distribution of equilateral triangles. b) Concept sketch of saturated (gray) and de-saturated triangular capillaries for increasing pressure levels (1), (2) and (3), e.g., during drainage.

519
520

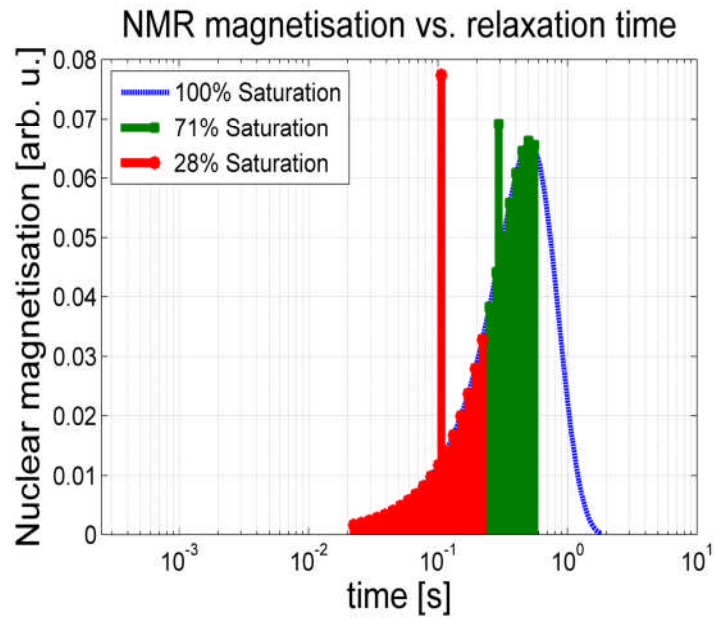


Figure 13: Relaxation components of fully (blue line) and partially de-saturated triangular pore size distribution. At a specific saturation level all pore corners with residual saturation exhibit the same NMR magnetization and relaxation behavior, thus superposing to a single fast relaxation component (e.g. red and green bars)

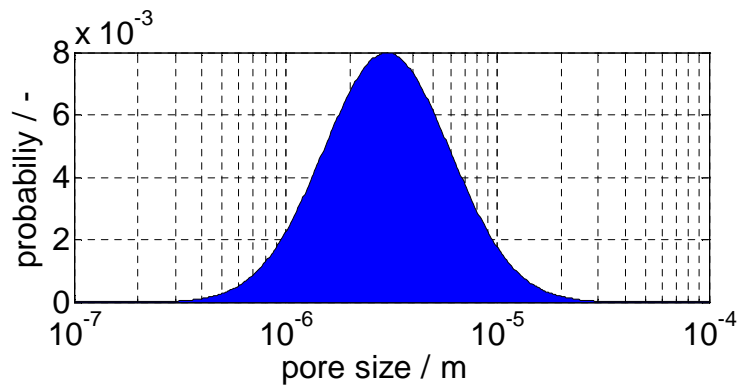


Figure 14. Pore-size distribution model (log-normal distribution: $\sigma = 0.3, \mu = 3 \mu m$) in analogy to that of the Rotliegend Sandstone shown in Fig. 2.

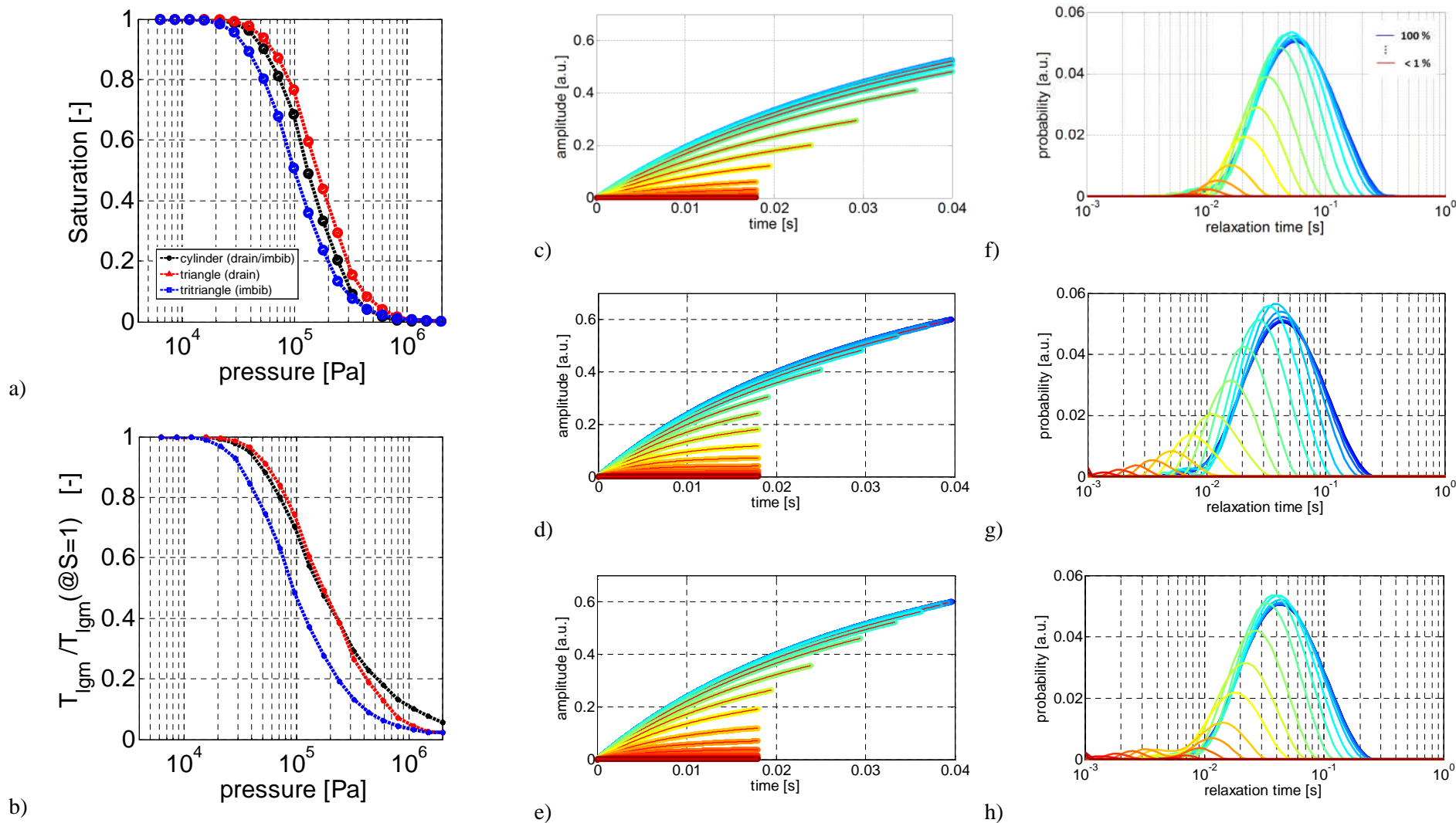


Figure 15: a) Modeled drainage and imbibition curves for circular and equilateral triangular capillary ensemble (cf Figure 14) and b) Corresponding normalized mean NMR T_1 relaxation times vs pressure curves. Modeled and fitted (red lines) NMR transient signals (longitudinal magnetization evolution) corresponding inverted NMR T_1 relaxation time distributions for 20 fully and partially saturated pore-size distributions ranging from < 1 % to 100 % saturation using circular (c, f) and equilateral triangular capillaries during imbibition (d, g) and drainage (e, h).

